https://doi.org/10.5194/egusphere-2026-2096
Preprint. Discussion started: 21 July 2026

Data-Driven Quadrature for Longwave and Shortwave Absorption by Major Greenhouse Gases

Paulina Czarnecki[1,2] and Manfred Brath[3]

[1]Department of Applied Physics and Applied Mathematics, Columbia University, New York, USA
[2]*now at* Institut Pierre-Simon Laplace, Sorbonne Université, Paris, France
[3]Meteorological Institute, Center for Earth System Research and Sustainability (CEN), Universität Hamburg, Hamburg, Germany

Correspondence: Paulina Czarnecki (pc2943@columbia.edu)

Abstract. Broadband radiation calculations are computationally expensive, and climate and weather models require fast parameterizations for computing the flow of energy through Earth's atmosphere. Data-driven quadrature is an alternative to traditional gas-optics parameterizations consisting of an optimal, sparse sample of representative spectral points (frequencies) and weights such that the weighted sum of monochromatic calculations approximates the broadband quantity, offering flexibility while maintaining the accuracy and efficiency of state-of-the-art schemes. Data-driven quadrature was originally developed in cloudless present-day conditions for longwave (thermal) radiation. In this work, we update the optimization algorithm to support shortwave (sunlight) calculations, which must be robust to variations in solar zenith angle and surface reflectivity. We additionally expand both the longwave and shortwave schemes to capture variability in major greenhouse gas concentrations, with potential application to different climate scenarios. The schemes are validated using ERA5 data with clear and cloudy skies and compared to a state-of-the-art radiation parameterization, showing comparable accuracy at lower computational cost. Furthermore, implementation in a single-column radiative-convective equilibrium model with interactive ozone chemistry demonstrates the versatility of the scheme and potential for online operationalization in dynamical models. Here we release and describe these optimized sets of quadrature points and associated weights, along with a tutorial to guide the optimization of new point and weight configurations for other applications.

1 Introduction

The flow of electromagnetic energy through the atmosphere sets Earth's energy balance. Atmospheric constituents including gases, aerosols, and clouds mediate the flow of radiation by absorbing, reflecting, and scattering sunlight (shortwave) and thermal (longwave) energy. Radiative transfer codes can be used in conjunction with Earth system models and satellite observations to accurately compute radiative fluxes and heating rates in order to study the interactions between radiation, the atmosphere, and the surface. However, these calculations are complicated by the strong dependence of the optical properties of atmospheric constituents on the spectral dimension (here, wavenumber).

At very high spectral resolution, radiative quantities can be computed to near-arbitrary accuracy by performing monochromatic (per wavenumber) radiative transfer calculations with line-by-line (LBL) codes (e.g., Buehler et al., 2025). Line-by-line

https://doi.org/10.5194/egusphere-2026-2096
Preprint. Discussion started: 21 July 2026

calculations, however, are incredibly computationally expensive and so unsuitable for atmospheric modeling. Thus radiation parameterizations aim to maintain accuracy while optimizing computational efficiency. The state-of-the-art parameterization commonly used in climate and weather models is the correlated-k distribution (Fu and Liou, 1992; Lacis and Oinas, 1991; Goody et al., 1989), which sorts absorption coefficients k, creating monotonic spectral integrals that can be evaluated at a sparse set of spectral points. While efficient and accurate, correlated-k distributions are often hand-tuned by experts (Hogan and Matricardi, 2020, 2022; Pincus et al., 2019), making them difficult to understand, use, and develop. Due to this tuning, they tend to be inflexible to large variability in greenhouse gases, including those present on exoplanets or in paleoclimate scenarios, updates to spectroscopy, and spectral overlap by greenhouse gases (Amundsen et al., 2017).

In Czarnecki et al. (2023), we develop an alternative spectral integration scheme, called data-driven quadrature (DDQ), with the goal of maintaining the accuracy and efficiency of correlated-k distributions while improving on transparency and flexibility. Our method directly samples the spectrum to find a sparse, optimal set of monochromatic fluxes and associated weights such that their weighted sum can accurately estimate radiative fluxes, heating rates, and top-of-the-atmosphere (TOA) forcing by CO_2. We find errors and computational expense, measured by the number of spectral points, commensurate with correlated-k models in longwave, clear-sky conditions.

In this followup work, we make strides towards operationalization as we expand the method to shortwave absorption, encompassing variability in solar zenith angle and surface reflectivity while keeping the size of the training dataset tractable. Additionally, in both the shortwave and the longwave, we optimize for variability in six major greenhouse gases beyond present-day concentrations. Here we release these quadrature points and weights along with a Python tutorial that may be used to generate new sets of quadrature points for different contexts. We validate the schemes extensively offline, comparing to the popular correlated-k distribution RRTMGP (Pincus et al., 2019) in both all-sky and clear-sky conditions. We also show good performance online with the implementation of DDQ as a gas optics scheme in the single-column radiative-convective equilibrium model `konrad` (Kluft et al., 2019), where DDQ tracks line-by-line calculations closely. Together with the tutorial, these new quadrature configurations allow for the broad implementation of DDQ as a gas optics scheme in climate and weather modeling applications.

2 Optimization Procedure

Details of the optimization of quadrature weights and points can be found in Czarnecki et al. (2023), Buehler et al. (2010), and Moncet et al. (2008). We revisit them briefly here.

The net broadband radiative flux at height z in the atmosphere, $F(z)$, is given by integrating monochromatic fluxes across the shortwave or the longwave spectrum:

$$F(z) = \int F_\nu(z)\,d\nu \approx \sum_i F_{\nu_i}(z)\Delta\nu_i, \tag{1}$$

where ν denotes wavenumber and $F_\nu(z) = F_\nu^\downarrow(z) - F_\nu^\uparrow(z)$ is the monochromatic net flux. Rather than calculating the integral directly via an existing quadrature method (e.g., the Riemann sum) that would require fine spectral discretization, we seek to

https://doi.org/10.5194/egusphere-2026-2096
Preprint. Discussion started: 21 July 2026

sparsely sample the spectrum to recover a small set of representative wavenumbers and associated quadrature weights. The weighted sum of monochromatic net flux at these representative wavenumbers approximates the full integral. As such, we rewrite Eqn. 1 as:

$$F(z) \approx \sum_{\nu \in S} w_\nu F_\nu(z), \tag{2}$$

where w_ν is the weight corresponding to wavenumber ν in the sparse subset S. The subset S is selected using a combinatorial optimization algorithm called simulated annealing (Kirkpatrick et al., 1983), the weights w are fit using a constrained linear regression, and both minimize the same cost function C. The software to solve this general optimization problem with user-defined cost functions and training data is openly available as Python package `datadrivenquadrature`.

2.1 Training Data

In order to inform the spectral sampling, we need fine-resolution monochromatic line-by-line calculations as well as corresponding integrated fluxes and heating rates throughout the atmosphere. Atmospheric profiles used for training must be sufficiently independent to allow for the matrix inversion necessary in the linear regression step while providing a representative sample of conditions for a given application.

To this end we adopt the set of atmospheric profiles developed for the Correlated K-Distribution Model Intercomparison Project (CKDMIP; Hogan and Matricardi, 2020), which span the present-day means, minima, and maxima in water vapor concentration, ozone concentration, and temperature. One hundred such profiles are available, and 50 are used for training and 50 for independent testing. We use the line-by-line code ARTS (Atmospheric Radiative Transfer Simulator; Buehler et al., 2025) to generate detailed spectral and broadband net fluxes. Heating rates, or flux divergence profiles, are computed from fluxes using a simple second-order accurate centered difference derivative matrix. One important update from Czarnecki et al. (2023) is that we increase vertical resolution at the expense of spectral resolution, training on 72,000 wavenumbers in the longwave and 62,000 in the shortwave. This is sufficient spectral detail to maintain accuracy to CKDMIP's original 7 million longwave wavenumbers, while the resulting free memory allows for training on each vertical model level, improving the prediction and generalization of heating rates.

In order to capture variability in six major greenhouse gases (CO_2, CH_4, O_3, N_2O, and additionally CFC-11 and -12 in the longwave), we perturb the concentration of each of these gases by a factor of 8 in each profile. Note that in the CKDMIP dataset, the concentrations of CFC-11 are scaled to include other ozone-depleting substances, a common procedure in radiation parameterization (Hogan and Matricardi, 2020).

Furthermore, in the shortwave, radiative transfer depends on the solar zenith angle and the optical properties of the surface. To account for these axes, each atmospheric profile is generated with five broadband surface reflectivities equally spaced from 0.15 to 0.75, as well as five solar zenith angles equally spaced in their cosine from 0.1 to 0.9. In order to facilitate the computation of linear weights by maintaining a small and linearly independent set of training profiles, solar zenith angle and surface reflectivity are randomly chosen for each of the 50 profiles at each optimization step.

https://doi.org/10.5194/egusphere-2026-2096
Preprint. Discussion started: 21 July 2026

The ARTS module `FluxSimulator` that may be used to perform line-by-line computations is available at https://github.com/atmtools/pyarts-fluxes, and the creation of training profiles is demonstrated in the included tutorial.

2.2 Cost Functions

The selection of the training profiles defines what variability in conditions we are interested in capturing; in contrast, the cost function determines which radiative quantities we demand accuracy in. We have previously shown that important quantities must be included in the cost function (Czarnecki et al., 2023). Very generally, the cost function used in all calculations can be defined as

$$C = f_0\|F_{est} - F_{ref}\| + f_1\|H_{est} - H_{ref}\| + \sum_i f_i\|\mathcal{F}^i_{est} - \mathcal{F}^i_{ref}\|. \tag{3}$$

The first term is the root-mean-squared error (RMSE) in net flux profile weighted by an empirically-derived scaling constant $f_0 = 0.15$. The second term is the RMSE in heating rate profile, with $f_1 = 1$. The final term is the RMSE in TOA radiative forcing $\mathcal{F} = \mathcal{F}^{TOA}_{present} - \mathcal{F}^{TOA}_{8\times i}$, with $i \in \{CO_2, CH_4, O_3, N_2O, \text{CFC-11}, \text{CFC-12}\}$. To train for present-day computation only, we set $f_i = 0$; for the limited climate change case with only CO_2 radiative forcing, $f_{CO_2} = 1$ (Czarnecki et al., 2023). To capture variability in all greenhouse gases in the longwave, $f_i = 1$ for all i; in the shortwave, CFC-11 and -12 do not exert a forcing and so their coefficients $f_{CFC-11} = f_{CFC-12} = 0$. Adding the forcing by each gas to the cost function provides information about how the spectrum changes with gas concentration, driving representative spectral points to important absorption bands. The scaling coefficients can be adjusted if necessary (e.g., if training a quadrature scheme for exoplanet applications).

This cost function, written to be compatible with the `datadrivenquadrature` optimization package, is available in the tutorial.

3 Quadrature Points and Weights

We describe the following sets of quadrature points and weights (available online; Czarnecki and Brath (2026)):

- `DDQ_LW_present`: 64 weights and points that perform the longwave spectral flux integral, trained on present-day variability in ozone, water vapor, and temperature, and 8 × CO_2 forcing;
- `DDQ_LW`: 64 weights and points that perform the longwave spectral flux integral, including variability in 6 major greenhouse gases;
- `DDQ_SW_present`: 64 weights and points that perform the shortwave spectral flux integral with present-day gas concentrations and CO_2 forcing, including variability in solar zenith angle and surface reflectivity;
- `DDQ_SW`: 64 weights and points that perform the shortwave spectral flux integral including variability in 4 major greenhouse gases, surface reflectivity, and solar zenith angle.

https://doi.org/10.5194/egusphere-2026-2096
Preprint. Discussion started: 21 July 2026

We perform 10 independent optimizations for each set of conditions described above. As the spread in final cost function values C is small, we validate only one DDQ configuration in this paper, chosen to best balance the terms of the cost function. However, we release all 10 optimizations, as this balance may be different across optimizations (e.g., favoring ozone optimization in the shortwave where the forcing is large) and users may wish to explore other configurations for their own applications.

In addition to these, other versions of DDQ are already publicly available, including present-day versions of both shortwave and longwave quadrature schemes that were released with the latest version of ARTS (Buehler et al., 2025) and limited versions of both longwave and shortwave schemes available as an optional gas-optics implementation in the single-column radiative-convective equilibrium model `konrad` (Kluft et al., 2019). The latter implementation includes idealizations made for the single-column model, such as a scaled insolation term for diurnally-averaged radiation calls and a single average surface reflectivity value, highlighting the flexibility of the method for different applications.

3.1 DDQ for Longwave Spectral Integration

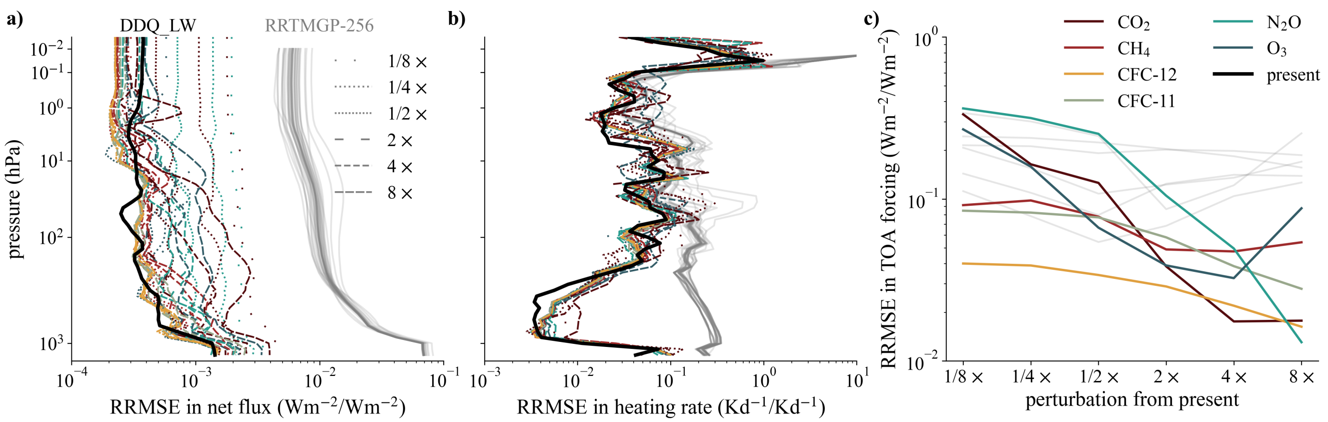

Figure 1. Relative root mean squared errors for **a)** net flux profiles, **b)** heating rate profiles, and **c)** top-of-the-atmosphere instantaneous radiative forcing in the CKDMIP testing dataset. Errors for `DDQ_LW` are shown in color, with each color denoting a single-gas perturbation and each linestyle encoding the size of the perturbation; the equivalent calculations for the correlated-k distribution RRTMGP are shown in grey to provide context. Errors at present-day concentrations, calculated using the limited configuration `DDQ_LW_present`, are shown in black.

We first validate `DDQ_LW_present` and `DDQ_LW` across a wide range of atmospheric conditions by calculating relative root mean squared error (with a floor of 0.1 in order to prevent artificial error amplification in regions with small reference values) in Figure 1. The mean is taken across the 50 clear-sky testing profiles in each single-gas perturbation scenario. The same calculations are shown for the popular correlated-k distribution RRTMGP-256, with 256 spectral points or g-points in the longwave. Our configurations of DDQ use 64 spectral points. DDQ boasts errors that are at worst similar to those of RRTMGP in flux profiles (Fig. 1a), heating rate profiles (Fig. 1b), and TOA forcing in atmospheres with $1/8\times$ to $8\times$ present-

https://doi.org/10.5194/egusphere-2026-2096
Preprint. Discussion started: 21 July 2026

day concentrations of individual greenhouse gases (Fig. 1c). DDQ heating rate errors are largest above the tropopause. Though DDQ extrapolates well outside of training conditions compared to correlated-k distributions (see 16 $\times$ CO_2 forcing, Fig. 6, Czarnecki et al. (2023)), accuracy is more limited outside of training conditions: forcing errors are larger at fractions of present-day concentrations, as the schemes are trained on $8\times$ present-day concentrations. This could be improved by increasing the span of training conditions.

3.2 DDQ for Shortwave Spectral Integration

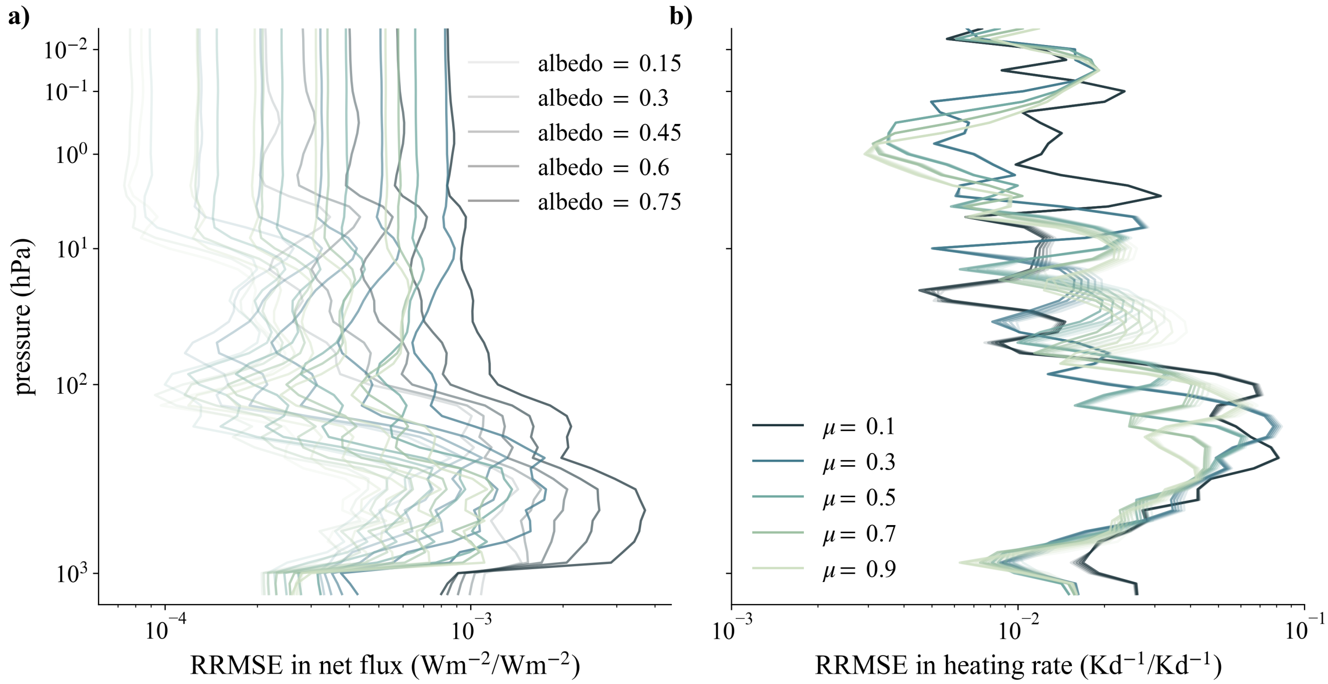

Figure 2. Relative root mean squared errors for **a)** net flux profiles and **b)** heating rate profiles in `DDQ_SW_present`. Error is grouped by the cosine of the solar zenith angle μ, illustrated with line color, and albedo, encoded by the saturation of the color. The plot demonstrates that though there is some spread in error across solar and surface conditions, both the spread and the total error are small.

In the shortwave, the DDQ scheme must be robust to changes in surface reflectivity or albedo, and solar zenith angle. Figure 2 shows how relative root mean squared error in flux profile (Fig. 2a) and heating rate (Fig. 2b) varies across solar and surface conditions in the quadrature configuration `DDQ_SW_present`. In both heating rates and fluxes, errors are larger at small $\mu = \cos(\text{sza})$ (higher solar zenith angles). Nonetheless, though there is some spread in the flux profiles across solar zenith angle, the worst-case error remains small; heating rate profile errors have much smaller spread and are likewise small. Thus in the validation of `DDQ_SW`, we take the mean of the error across solar zenith angle and surface albedo in order to produce a cleaner plot, with confidence that we are not missing any biases due to varying boundary conditions. Note that DDQ is both

https://doi.org/10.5194/egusphere-2026-2096
Preprint. Discussion started: 21 July 2026

tested and trained on a scalar surface reflectivity here; the impact of spectrally-resolved surface reflectivity will be explored in Section 3.3.

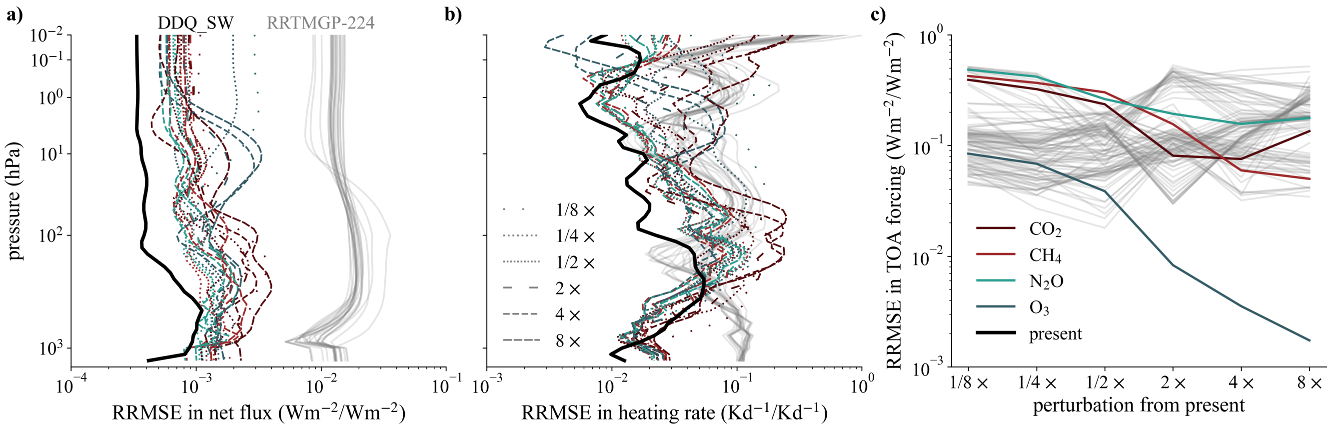

Figure 3. Relative root mean squared errors for **a)** net flux profiles, **b)** heating rate profiles, and **c)** top-of-the-atmosphere instantaneous radiative forcing in the CKDMIP testing dataset. Errors for `DDQ_SW` are shown in color, with each color denoting a single-gas perturbation and each linestyle encoding the size of the perturbation; the equivalent calculations for the correlated-k distribution RRTMGP are shown in grey to provide context. Errors at present-day concentrations, calculated using the limited configuration `DDQ_SW_present`, are shown in black.

As before, we validate `DDQ_SW_present` and `DDQ_SW` across a wide range of clear-sky atmospheric conditions by calculating relative root mean squared error, averaging over solar zenith angle and surface albedo, in Figure 3. The same calculations are shown for RRTMGP-224, which has 224 spectral points in the shortwave. Note that here, for each gas perturbation, we average over a sample of 10 of the 50 reference profiles to keep the number of line-by-line reference calculations required computationally tractable. DDQ errors remain comparable to those of RRTMGP in flux profiles (Fig. 3a), heating rate profiles (Fig. 3b), and TOA forcing in atmospheres with $1/8\times$ to $8\times$ present-day concentrations of individual greenhouse gases (Fig. 3c). Shortwave heating rate errors are relatively larger than longwave above 500 hPa as compared to RRTMGP-224 but remain small at about 0.1 K/day. DDQ has larger forcing errors in CO_2, CH_4 and N_2O forcing than O_3 because these forcings are very small in the shortwave and thus O_3 is prioritized in the optimization; if desired this could be remedied by modifying the coefficients f_i in the cost function (Eqn. 3). Nonetheless, we show RRTMGP error separately across solar and surface variables to show that mean `DDQ_SW` error lies within the spread of RRTMGP errors; in individual profiles, DDQ error may be larger. As in the longwave, our configurations of DDQ use 64 spectral points, which is much sparser than this implementation of RRTMGP with 224 g-points.

https://doi.org/10.5194/egusphere-2026-2096
Preprint. Discussion started: 21 July 2026

3.3 Extrapolation to Clouds: Validation in ERA5 Reanalysis Data

In this section we validate the DDQ scheme for all-sky conditions. Using ERA5 reanalysis data, we run simulations for all-sky conditions estimating the radiative fluxes and heating rates using the DDQ scheme and compare them with reference line-by-line simulations, both using ARTS 2.6.15.

The ERA5 data consists of a snapshot of the atmosphere from 01/08/2022 09:00:00 UTC, with a horizontal resolution of 1 degree and 137 vertical levels from 4D variational analysis. The data among other variables includes temperature, humidity, ozone, and hydrometeor contents. Included gases are H_2O, O_2, N_2, O_3, CO_2, N_2O and CH_4. H_2O and O_3 concentrations are taken from the ERA5 data, while CO_2, N_2O, O_2 and CH_4 are set to their present-day concentrations.

Gas absorption is taken into account by using ARTS' line-by-line data, which is based on the HITRAN (Gordon et al., 2022) database; MT_CKD for continuum absorption (version 3.5 for H_2O and version 2.5.2 for CO_2 (Mlawer et al., 2012)); collision-induced absorption (version 1.0 for O_2 and version 2.5.2 for N_2); and the ARTS cross-section catalog for ozone. The ozone cross-section data is derived from Gorshelev et al. (2014) and Serdyuchenko et al. (2014) using the `arts-crossfit` package (Buehler et al., 2022). Molecular scattering is taken into account by using the Rayleigh phase matrix including polarization from Hansen and Travis (1974) with a depolarization factor of 0.03 and the Rayleigh cross-section parameterization from Stamnes et al. (2017) and Bates (1984). For details, see Brath et al. (2024).

Four different hydrometeor types are included, each with its own particle size distribution: cloud liquid water, cloud ice, rain and snow. Rain and cloud liquid water are assumed to be liquid water spheres, and the scattering data is taken from the `arts-xml-data` package (version 2.6.14). Cloud ice is assumed as hexagonal columns, snow as 10-plate-aggregate and graupel as droxtal from the scattering database of Yang et al. (2013) and Bi and Yang (2017). The scattering database converted to the ARTS single scattering data format is freely available from Zenodo (https://doi.org/10.5281/zenodo.10807525; Eriksson and Barlakas (2024)).

The surface data is estimated from daily global surface reflectances from the MYD09CMG Version 6.1 product from June to July 2022. It provides estimated surface spectral reflectances of Aqua MODIS at 0.05 degree resolution. Due to a limitation of the CDISORT implementation in ARTS, all surfaces are assumed to be Lambertian (Brath et al., 2024).

For the thermal reference simulations the spectrum is sampled linearly between 10 and 5,000 cm^{-1}, and logarithmically between 1,000 and 100,000 cm^{-1} for the solar reference simulations, each with 10,000 frequency points. The sun is overhead at 18 degrees north and 45 degrees east, which roughly corresponds to the location of the sun at the simulation time.

3.3.1 Fluxes

First, we analyze the fluxes at the top of the atmosphere (TOA) and at the surface for longwave and shortwave separately for clear-sky and all-sky conditions. The globally-averaged upward and downward reference fluxes at TOA and at the surface for longwave and shortwave radiation are shown in Table 1. The differences from the reference fluxes for the `DDQ_LW` and `DDQ_SW` sets are shown in Table 2.

https://doi.org/10.5194/egusphere-2026-2096
Preprint. Discussion started: 21 July 2026

Radiation Type and Case	TOA up [Wm^{-2}]	TOA down [Wm^{-2}]	SFC up [Wm^{-2}]	SFC down [Wm^{-2}]
all-sky solar	130.821	339.988	16.8471	154.165
clear-sky solar	23.3143	339.988	25.4359	270.883
all-sky thermal	225.027	0	412.063	371.771
clear-sky thermal	269.576	0	409.691	324.331

Table 1. Reference flux values for longwave and shortwave radiation (W/m^2).

Setup	TOA up [Wm^{-2}]	TOA down [Wm^{-2}]	SFC up [Wm^{-2}]	SFC down [Wm^{-2}]
		All-Sky Conditions		
`DDQ_LW`	-0.9894	0	1.5407	1.6628
`DDQ_LW_present`	-0.1574	0	-0.974	-0.708
`DDQ_SW`	-2.3849	-1.6807	-0.1719	-1.2091
`DDQ_SW_present`	-3.8506	-1.4804	-0.6375	-2.4441
		Clear-Sky Conditions		
`DDQ_LW`	-1.4299	0	1.5484	1.8162
`DDQ_LW_present`	-0.2565	0	-0.963	-0.4876
`DDQ_SW`	-0.2467	-1.6807	-0.2521	-0.9754
`DDQ_SW_present`	-0.8817	-1.4804	-0.9528	-0.7194

Table 2. Difference between DDQ configurations and reference simulations (W/m^2).

Both DDQ longwave schemes reproduce the reference longwave fluxes at TOA. They deviate by less than 0.5 % at TOA for the upward fluxes and by less than 0.6 % at the surface for the upward and downward fluxes. A deviation of 0.5 % corresponds roughly to 1 W/m^2, which is the order of deviation that can be expected even from comparison with reference radiative transfer models (Pincus et al., 2015). The shortwave deviations are larger than the longwave. At the TOA, the upward all-sky shortwave flux differs by 2 % for the `DDQ_SW` set and by 3 % for the `DDQ_SW_present` set. In clear-sky conditions, they differ by about 1 % and 4 %, respectively. At the surface, the downward flux differs by about 1 % for both DDQ sets in all-sky conditions. For clear-sky conditions, the `DDQ_SW` sets differ by less than 0.4 %. The upward flux at the surface differs for all-sky and clear-sky conditions by 1 % for the `DDQ_SW` set and by 4 % for the `DDQ_SW_present` set. In clear-sky conditions, the surface is the main source of the deviations, especially for the `DDQ_SW_present` set, as both are trained on spectrally-constant surface reflectivities and tested on spectrally-resolved surface reflectivities. Conversely in all-sky conditions, the influence of the surface is partially masked by the clouds. Locally, the upward flux deviates up to 20 % for the `DDQ_SW_present` set (Fig. 4b). For the `DDQ_SW` set the deviations are mostly below 10 % (Fig. 4c). The strongest deviations occur at regions where the actual upward surface flux is small (Fig. 4a). On the global scale, most of the deviations at the surface cancel out.

https://doi.org/10.5194/egusphere-2026-2096
Preprint. Discussion started: 21 July 2026

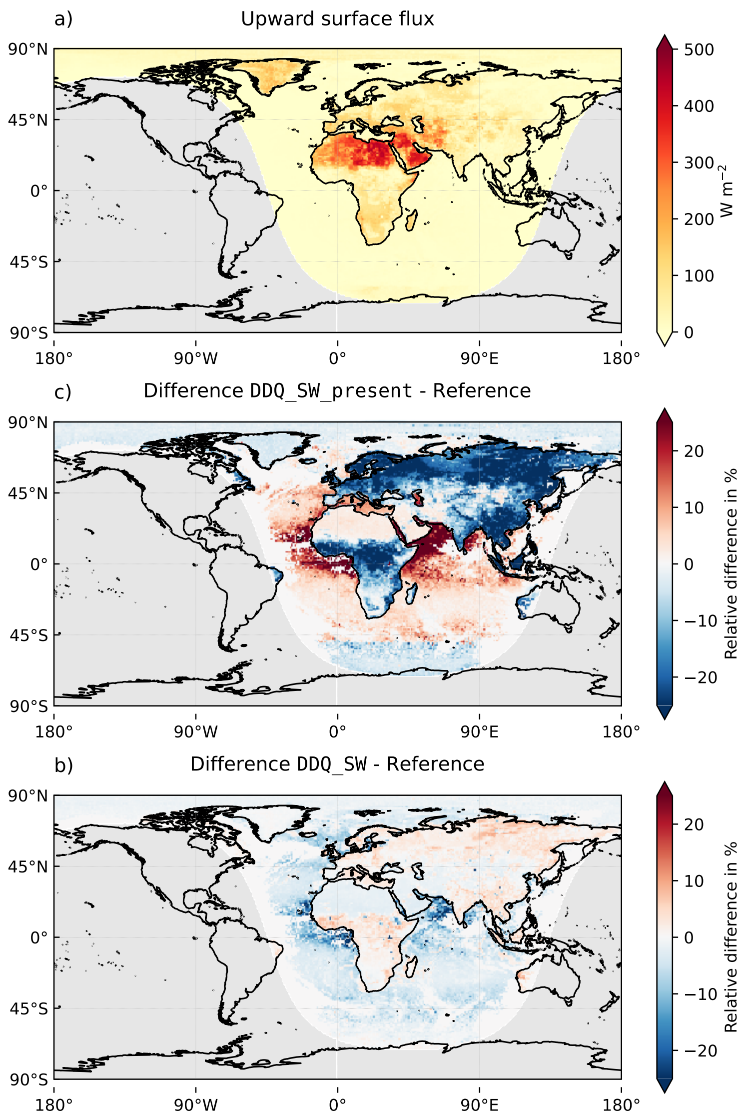

Figure 4. Solar upward flux at the surface for all-sky conditions. The grey shading marks the night side, where no sunlight is present. Panel **a)** shows the reference simulation, panel **b)** the flux as generated by the `DDQ_SW` set, and panel **c)** the `DDQ_SW_present` set. In panels **b)** and **c)** relative errors are only shown if the reference flux is higher than 1 Wm^{-2}.

3.3.2 Heating Rates

In this section, we analyze the heating rates first for the longwave and then for the shortwave. We will focus on all-sky conditions, as clear-sky conditions were already validated in the previous sections.

https://doi.org/10.5194/egusphere-2026-2096
Preprint. Discussion started: 21 July 2026

Fig. 5 shows the thermal heating rate distribution for the reference line-by-line simulation (Fig. 5a) and the density of deviations for the `DDQ_LW` (Fig. 5b) and `DDQ_LW_present` schemes (Fig. 5c). From the surface up to altitudes of 10 hPa, both `DDQ` sets are practically bias free and have deviations less than 0.2 $\mathrm{Kd^{-1}}$; the highest density of deviation lies at less than 0.1 $\mathrm{Kd^{-1}}$. From 10 hPa to 0.1 hPa, the root mean square deviation (RMSD) is about 1 $\mathrm{Kd^{-1}}$, which is mainly caused by a systematic deviation as seen by the non zero bias. Above 0.1 hPa, the deviation strongly increases. From a clear-sky test (not shown) with 20 times higher spectral resolution ($\Delta\tilde{\nu} = 0.025\ \mathrm{cm^{-1}}$), we know that for a spectral resolution of $\Delta\tilde{\nu} = 0.5\ \mathrm{cm^{-1}}$, the error of the heating rate is in the order of 1 $\mathrm{Kd^{-1}}$ to 2 $\mathrm{Kd^{-1}}$ at the stratopause (1 hPa) and even higher when considering the mesosphere. Therefore, we cannot determine if the deviations above the stratopause are caused by the spectral resolution of the reference simulation, by the DDQ scheme, or both. RRTMGP exhibits similar errors at high altitudes (Fig. 1).

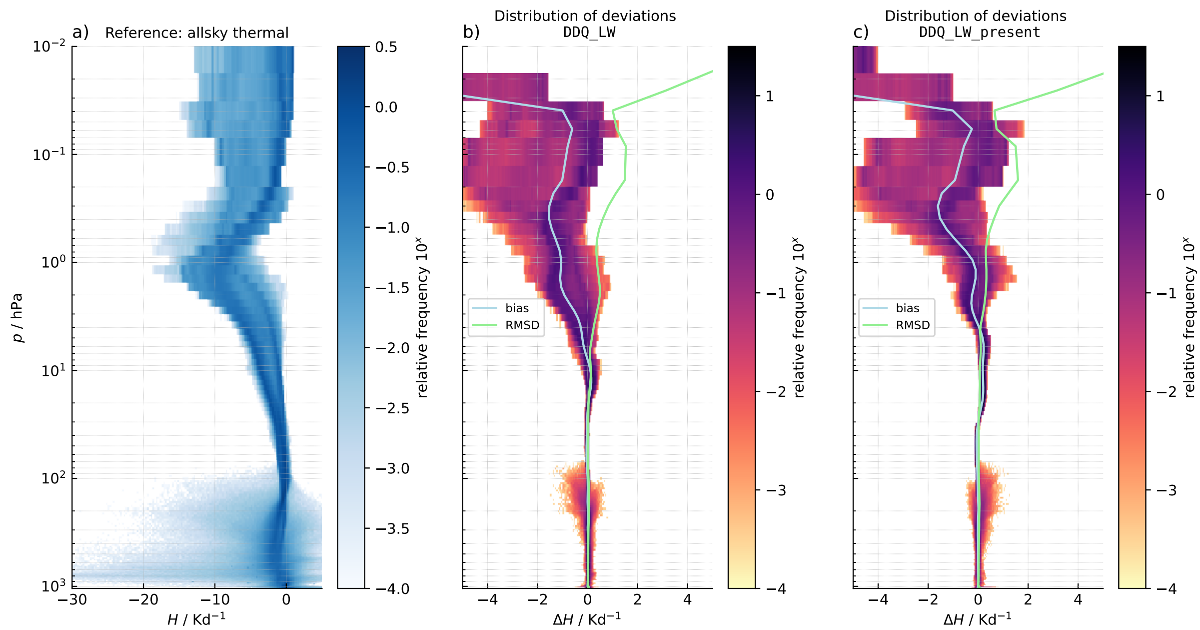

Figure 5. Longwave heating rate comparison in a snapshot of ERA5. Panel **a)** shows the reference LBL heating rate distribution; panel **b)** shows distributions of deviations for `DDQ_LW`, and panel **c)** tests the `DDQ_LW_present` set. For details, see text.

Fig. 6 shows the shortwave heating rate distribution for the reference line-by-line simulation (Fig. 6a) as well as the distributions of deviations for the `DDQ_SW` (Fig. 6b) and `DDQ_SW_present` sets (Fig. 6c). Both DDQ sets are similar above the tropopause (< 100 hPa), with biases in the order of 0.1 $\mathrm{Kd^{-1}}$ and RMSD on the order of 0.2 $\mathrm{Kd^{-1}}$ in the stratosphere. Above the stratosphere (< 1 hPa) the magnitude of both the bias and the RMSD increases to more than 1 $\mathrm{Kd^{-1}}$. The reason for this is that the `DDQ` sets miss some absorption features that are important for the heating rate in the mesosphere. In the troposphere (> 100 hPa) both `DDQ` sets are similar in terms of bias and RMSD. The bias is slightly larger in magnitude (up to 0.2 $\mathrm{Kd^{-1}}$) than in the stratosphere, but the RMSD increases strongly to about 0.7 $\mathrm{Kd^{-1}}$. The main difference between the two `DDQ` sets are the extreme values of their deviation distributions. The `DDQ_SW` configuration has negative deviations up to $-4\ \mathrm{Kd^{-1}}$, while

https://doi.org/10.5194/egusphere-2026-2096
Preprint. Discussion started: 21 July 2026

`DDQ_SW_present` exhibits values only down to $-1\,\mathrm{K\,d^{-1}}$. In contrast, `DDQ_SW_present` has more higher positive deviations than the `DDQ_SW` set. The higher heating rate deviations between 100 hPa and 300 hPa result from cloud absorption in the near infrared. Ice clouds have three strong absorption peaks in the near infrared (Warren, 2019), which are not captured well
230 enough by the `DDQ` sets. For liquid clouds, these deviations are much smaller, as the absorption peaks are less pronounced and the ice clouds, which mostly occur at higher altitudes, mask the interaction of the radiation with the liquid clouds. Nonetheless, RRTMGP's cloud-optics scheme does not explicitly consider these absorption peaks as cloud optics are computed as band- or g-point averages (Pincus et al., 2019), and the magnitude of DDQ's shortwave errors is similar to RRTMGP all-sky errors in the longwave (not shown). Thus we maintain that DDQ is suitable for most all-sky calculations.

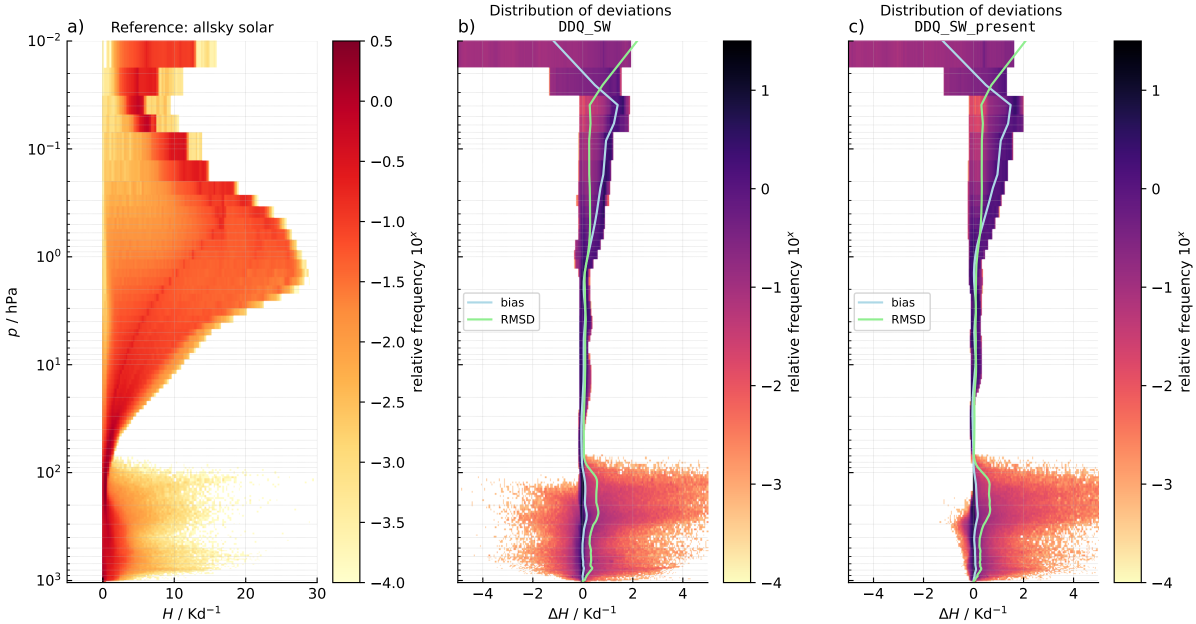

Figure 6. Shortwave heating rate comparison in ERA5. Panel **a)** shows the shortwave heating rate distribution for the reference line-by-line simulation; panel **b)** shows the density of deviations from the reference by `DDQ_SW`, while panel **c)** tests the `DDQ_SW_present` set. For details, see text.

235 ### 3.4 Atmospheric Chemistry: Interactive Ozone in `konrad`

Finally, we wish to explore the operationalization of DDQ as a gas optics scheme by testing its interaction with a linear ozone chemistry parameterization (Cariolle and Teyssedre, 2007) in the single-column radiative-convective equilibrium (RCE) model `konrad` (Kluft et al., 2019). Both line-by-line code ARTS and the quadrature scheme, which depends on ARTS to perform the monochromatic flux computations at the selected quadrature points, are implemented within `konrad`, allowing for direct
240 comparison.

https://doi.org/10.5194/egusphere-2026-2096
Preprint. Discussion started: 21 July 2026

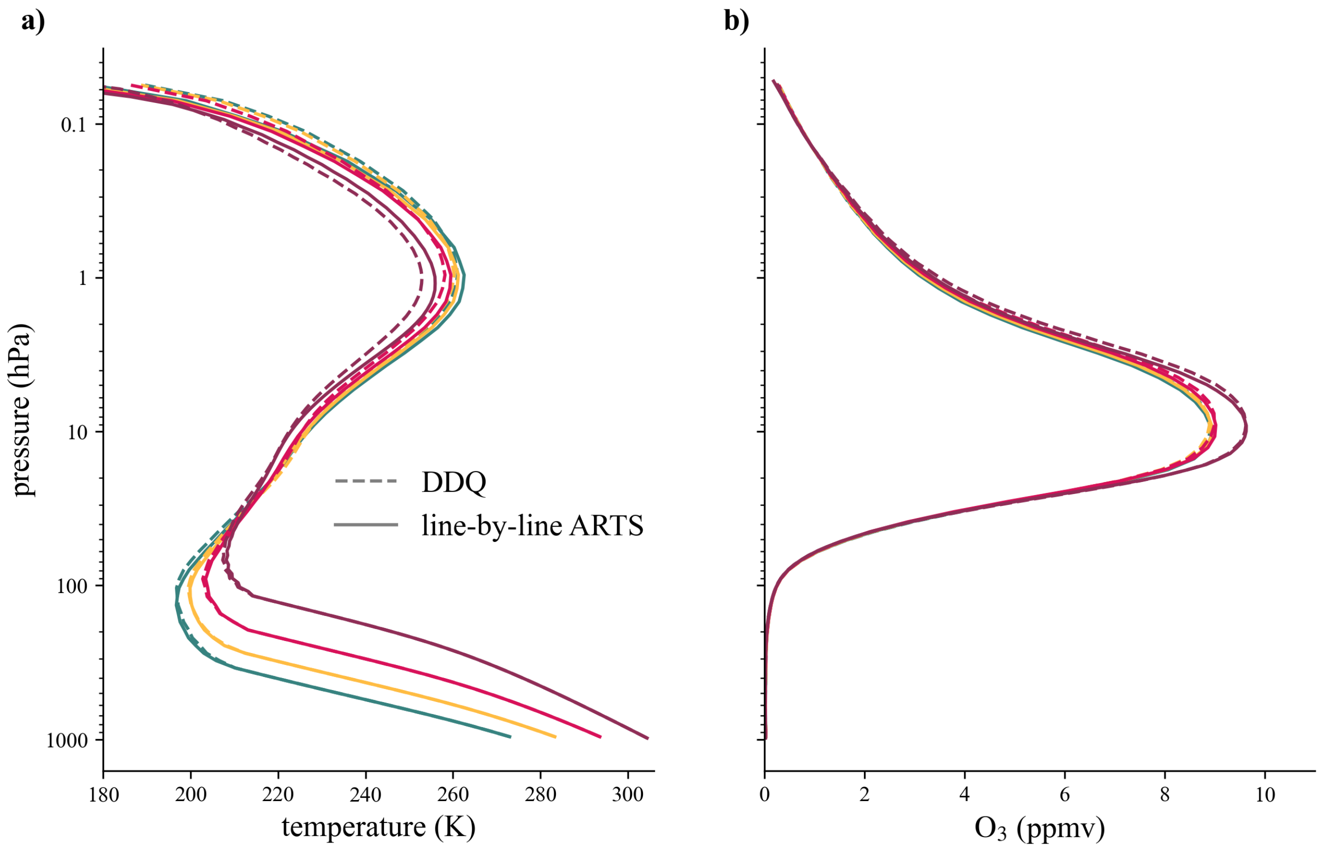

Figure 7. a) Temperature profiles and **b)** ozone concentration profiles for the equilibrium state of RCE model `konrad` including an interactive ozone scheme. Solid lines denote the use of line-by-line code ARTS as the radiation scheme, while dashed lines denote the use of `DDQ_SW` and `DDQ_LW`. The model is run for four fixed surface temperatures (275 K, teal; 285 K, yellow; 295 K, red; and 305 K, purple). The model converges to very similar states with both schemes.

The RCE model is run independently with both ARTS and DDQ as the radiation code across a set of fixed surface temperatures $T_s \in \{275, 285, 295, 305\}$ Kelvin with a 2-hour timestep and until convergence (with a maximum of 150 days). The vertical discretization is doubled (from 64 levels to 128) in the $T_s = 305$ K case to stabilize the numerical integration. To test the flexibility of DDQ to changing gas concentrations, the Cariolle interactive ozone scheme is used (Cariolle and Teyssedre, 2007). In Figure 7, the equilibrium RCE state, as defined by the temperature profile (Fig. 7a) and the ozone concentration profile (Fig. 7b) is shown. The states resulting from `konrad` with DDQ as the radiation scheme (dashed lines) are very similar to those from line-by-line radiation (solid lines), and any discrepancies are within the bias of the default radiation scheme RRTMG (not shown). Though `konrad` is a single-column model with many simplifications, the accuracy and stability of DDQ in this setting show promise for further operationalization in more complex models.

https://doi.org/10.5194/egusphere-2026-2096
Preprint. Discussion started: 21 July 2026

4 Summary and Discussion

In this work, we advance data-driven quadrature towards operationalization. While originally developed in longwave, present-day, clear-sky conditions, DDQ has been extended to shortwave radiation calculations with variability across solar zenith angles and surface reflectivities. DDQ can also flexibly maintain accuracy across variability in the concentrations of six major greenhouse gases. We extensively validated four quadrature configurations against line-by-line code ARTS and compared to state-of-the-art gas-optics scheme RRTMGP. The quadrature schemes maintain efficiency and accuracy in a wide range of gas concentrations as well as in clear-sky and all-sky ERA5 snapshots. Finally, we test an online implementation in a simple model with an interactive ozone parameterization, further highlighting the versatility of the scheme and the potential for implementation in larger models.

The major limitation of DDQ is its dependence on the breadth of training conditions used; as is true for all optimization methods, extrapolation to novel conditions is limited and users may wish to train DDQ configurations specifically to their use cases. To this end, along with these four quadrature scheme configurations, consisting of quadrature points and associated weights, we release a Python tutorial that may be used to train a new quadrature scheme. Users may wish to train a new configuration for specific applications (for exoplanets with vastly different gas concentrations), for a specific model (for best results, the vertical grid of the training data should match a given model, as extrapolation in pressure proves to be difficult; c.f. Fig. 4 in Czarnecki et al. (2023)), or to focus on a limited set of conditions to increase efficiency (for a simple model, training on limited gas variability may decrease the number of spectral points necessary as it decreases the complexity of the information learned).

Additional validation will be performed within a dynamical model, to ensure the parameterized radiation interacts realistically with atmospheric dynamics. For the full operationalization of DDQ in an Earth system model, a procedure to generate monochromatic fluxes must be devised, as the quadrature scheme relies on monochromatic flux calculations ahead of spectral integration. Currently, this is achieved with the line-by-line code ARTS (e.g., within `konrad` or the `FluxSimulator` module), though this is impractical for implementation in larger models. Absorption coefficients for gas-optics schemes are typically stored in lookup tables across a wide range of temperatures and pressures; at each radiation call in the model integration, these absorption coefficients are looked up, optical depth is calculated, and then the equations of radiative transfer are solved. This is a potential avenue for the implementation of DDQ, though lookup tables are bulky and the monochromatic nature of DDQ lends itself to further optimization of this step. Instead, reference absorption coefficients could be stored and then interpolated for pressure and temperature. The interpolation function could be fit by training a neural network (or, in the simplest case, a linear spline), reducing the lookup operation to a polynomial or linear function call. This would further increase the efficiency of the radiation calculation, which is already competitive with state-of-the-art parameterizations.

With the DDQ tutorial in hand, one may wish to include additional components in the gas optics scheme. One such component may include the separate computation of photosynthetically-active radiation (PAR), a shortwave spectral band important for atmosphere-biosphere coupling. The spectral sampling of the PAR band in particular has been shown to be important to the estimation of gross primary productivity and thus carbon sequestration by plants, motivating DDQ as an appropriate approach

https://doi.org/10.5194/egusphere-2026-2096
Preprint. Discussion started: 21 July 2026

(Clevers and Kooistra, 2011; Gates et al., 1965). This may be achieved by including both the PAR and the broadband integral in the shortwave cost function, such that the quadrature scheme must include spectral points that correctly return both the band and the broadband integral. One may also wish to improve the representation of clouds; forcing sampling of spectral bands where ice, water, and mixed-phase clouds absorb and scatter light may minimize all-sky errors (Warren, 2019; Lu et al., 2011). This can be achieved by including all-sky profiles in the training dataset, or by including the atmospheric cloud radiative effect (the difference between heating in cloudy and clear skies) in the cost function.

Additionally, DDQ may be extended to learn further variability without increasing computational cost. One such extension is spectrally-varying surface albedo. While typically, surface albedo is taken to be a broadband constant (as in this work) or a set of coarsely band-averaged values in Earth system models (as in Section 3.3), including the spectral representation of the surface has been shown to be important in representing different land surface types, in particular snow and ice (Henderson-Sellers and Wilson, 1983). A DDQ configuration can be easily trained to make this improvement by sampling spectral, rather than broadband, surface conditions, as in our shortwave training; though the `DDQ_SW` configuration matches reference calculations using a spectral surface reflectivity fairly well, users may wish to re-train a DDQ configuration for a specific land-surface model, especially in a more limited `DDQ_SW_present` case.

Finally, the theory behind DDQ is based on a similar procedure for simulating hyperspectral satellite observations (Buehler et al., 2010; Moncet et al., 2008). Beyond applications in weather or climate models, a configuration of quadrature points can be easily trained on satellite retrievals to a similar end. Indeed, the Weighted-Mean of Representative Frequencies approach, including frequencies and associated weights for the HIRS (High Resolution Infrared Radiation Sounder) instrument, has long been included with releases of ARTS (Buehler et al., 2025, 2010). An existing infrastructure to simulate a user-defined instrument also exists. Thus combined with the included tutorial, it should be straightforward to develop broadband simulators for a wide range of instruments with ARTS. This simulator can then facilitate novel model-observation comparison, including via inexpensive online observation simulation within a global climate model.

Code and data availability. Code used to generate the figures and training datasets, cost functions used for the optimization algorithm, and quadrature points and associated weights, are available at https://doi.org/10.5281/zenodo.18958691 (Czarnecki and Brath, 2026). The optimization may be performed using the publicly-available Python package `datadrivenquadrature`. Atmospheric conditions used for training and testing are freely available from the CKDMIP project (Hogan and Matricardi, 2020). ERA5 data is available at the Copernicus Climate Store.

Author contributions. P.C. conceptualized the study and developed the DDQ model and tutorial. Both P.C. and M.B. performed the analysis, validated the model, created visualizations, and wrote the manuscript.

Competing interests. The authors declare no competing interests.

https://doi.org/10.5194/egusphere-2026-2096
Preprint. Discussion started: 21 July 2026

Acknowledgements. We would like to thank Neal Ma for implementing DDQ as a Python package. We are also grateful to Robert Pincus, Stefan Buehler, and Lukas Kluft for many helpful discussions about this work. P.C. was supported by the US National Science Foundation (award AGS 19-16908).

https://doi.org/10.5194/egusphere-2026-2096
Preprint. Discussion started: 21 July 2026

References

Amundsen, D. S., Tremblin, P., Manners, J., Baraffe, I., and Mayne, N. J.: Treatment of overlapping gaseous absorption with the correlated-k method in hot Jupiter and brown dwarf atmosphere models, Astronomy & Astrophysics, 598, A97, 2017.

Bates, D.: Rayleigh scattering by air, Planetary and Space Science, 32, 785–790, 1984.

Bi, L. and Yang, P.: Improved ice particle optical property simulations in the ultraviolet to far-infrared regime, Journal of Quantitative Spectroscopy and Radiative Transfer, 189, 228–237, 2017.

Brath, M., Petersen, J., Buehler, S. A., and Eriksson, P.: Extending the Atmospheric Radiative Transfer Simulator (Arts) to Shortwave Radiation, Available at SSRN: https://ssrn.com/abstract=4968132, https://doi.org/10.2139/ssrn.4968132, 2024.

Buehler, S., John, V., Kottayil, A., Milz, M., and Eriksson, P.: Efficient radiative transfer simulations for a broadband infrared radiometer, Journal of Quantitative Spectroscopy and Radiative Transfer, 111, 602–615, 2010.

Buehler, S. A., Brath, M., Lemke, O., Hodnebrog, Ø., Pincus, R., Eriksson, P., Gordon, I., and Larsson, R.: A New Halocarbon Absorption Model Based on HITRAN Cross-Section Data and New Estimates of Halocarbon Instantaneous Clear-Sky Radiative Forcing, Journal of Advances in Modeling Earth Systems, 14, e2022MS003 239, 2022.

Buehler, S. A., Larsson, R., Lemke, O., Pfreundschuh, S., Brath, M., Adams, I., Fox, S., Roemer, F. E., Czarnecki, P., and Eriksson, P.: The atmospheric radiative transfer simulator arts, version 2.6—Deep Python integration, Journal of Quantitative Spectroscopy and Radiative Transfer, p. 109443, 2025.

Cariolle, D. and Teyssedre, H.: A revised linear ozone photochemistry parameterization for use in transport and general circulation models: multi-annual simulations, Atmospheric chemistry and physics, 7, 2183–2196, 2007.

Clevers, J. and Kooistra, L.: Using hyperspectral remote sensing data for retrieving canopy chlorophyll and nitrogen content, IEEE JSTAR, 2011.

Czarnecki, P. and Brath, M.: Supplement to "Data-Driven Quadrature for Longwave and Shortwave Absorption by Major Greenhouse Gases" [dataset], https://doi.org/10.5281/zenodo.18958691, 2026.

Czarnecki, P., Polvani, L., and Pincus, R.: Sparse, empirically optimized quadrature for broadband spectral integration, Journal of Advances in Modeling Earth Systems, 15, e2023MS003 819, 2023.

Eriksson, P. and Barlakas, V.: Single scattering properties of ice hydrometeors between 0.2 and 99 um (Bi and Yang, 2017) [dataset], https://doi.org/10.5281/zenodo.10807525, 2024.

Fu, Q. and Liou, K.: On the correlated k-distribution method for radiative transfer in nonhomogeneous atmospheres, Journal of the Atmospheric Sciences, 49, 2139–2156, 1992.

Gates, D. et al.: Spectral properties of plants, Applied optics, 1965.

Goody, R., West, R., Chen, L., and Crisp, D.: The correlated-k method for radiation calculations in nonhomogeneous atmospheres, Journal of Quantitative Spectroscopy and Radiative Transfer, 42, 539–550, 1989.

Gordon, I., Rothman, L., Hargreaves, R., Hashemi, R., Karlovets, E., Skinner, F., Conway, E., Hill, C., Kochanov, R., Tan, Y., et al.: The HITRAN2020 molecular spectroscopic database, Journal of Quantitative Spectroscopy and Radiative Transfer, 277, 107 949, 2022.

Gorshelev, V., Serdyuchenko, A., Weber, M., Chehade, W., and Burrows, J. P.: High spectral resolution ozone absorption cross-sections – Part 1: Measurements, data analysis and comparison with previous measurements around 293 K, Atmospheric Measurement Techniques, 7, 609–624, 2014.

Hansen, J. E. and Travis, L. D.: Light scattering in planetary atmospheres, Space Science Reviews, 16, 527–610, 1974.

https://doi.org/10.5194/egusphere-2026-2096
Preprint. Discussion started: 21 July 2026

Henderson-Sellers, A. and Wilson, M.: Surface albedo data for climatic modeling, Reviews of Geophysics, 1983.

Hogan, R. J. and Matricardi, M.: Evaluating and improving the treatment of gases in radiation schemes: the Correlated K-Distribution Model Intercomparison Project (CKDMIP), GMD, 13, 6501–6521, 2020.

Hogan, R. J. and Matricardi, M.: A tool for generating fast k-distribution gas-optics models for weather and climate applications, Journal of Advances in Modeling Earth Systems, p. e2022MS003033, 2022.

Kirkpatrick, S., Gelatt Jr, C. D., and Vecchi, M. P.: Optimization by simulated annealing, Science, 220, 671–680, 1983.

Kluft, L., Dacie, S., Buehler, S. A., Schmidt, H., and Stevens, B.: Re-examining the first climate models: Climate sensitivity of a modern radiative–convective equilibrium model, Journal of Climate, 32, 8111–8125, 2019.

Lacis, A. A. and Oinas, V.: A description of the correlated k-distribution method for modeling nongray gaseous absorption, thermal emission, and multiple scattering in vertically inhomogeneous atmospheres, Journal of Geophysical Research: Atmospheres, 96, 9027–9063, 1991.

Lu, P., Zhang, H., and Li, J.: Correlated k-distribution treatment of cloud optical properties and related radiative impact, Journal of the atmospheric sciences, 2011.

Mlawer, E. J., Payne, V. H., Moncet, J.-L., Delamere, J. S., Alvarado, M. J., and Tobin, D. C.: Development and Recent Evaluation of the Mt_ckd Model of Continuum Absorption, Philosophical Transactions of the Royal Society A: Mathematical, Physical and Engineering Sciences, 370, 2520–2556, 2012.

Moncet, J.-L., Uymin, G., Lipton, A. E., and Snell, H. E.: Infrared radiance modeling by optimal spectral sampling, Journal of the Atmospheric Sciences, 65, 3917–3934, 2008.

Pincus, R., Mlawer, E. J., Oreopoulos, L., Ackerman, A. S., Baek, S., Brath, M., Buehler, S. A., Cady-Pereira, K. E., Cole, J. N. S., Dufresne, J.-L., Kelley, M., Li, J., Manners, J., Paynter, D. J., Roehrig, R., Sekiguchi, M., and Schwarzkopf, D. M.: Radiative flux and forcing parameterization error in aerosol-free clear skies, Geophysical Research Letters, 42, 5485–5492, https://doi.org/10.1002/2015GL064291, 2015.

Pincus, R., Mlawer, E. J., and Delamere, J. S.: Balancing accuracy, efficiency, and flexibility in radiation calculations for dynamical models, Journal of Advances in Modeling Earth Systems, 11, 3074–3089, 2019.

Serdyuchenko, A., Gorshelev, V., Weber, M., Chehade, W., and Burrows, J. P.: High spectral resolution ozone absorption cross-sections – Part 2: Temperature dependence, Atmospheric Measurement Techniques, 7, 625–636, 2014.

Stamnes, K., Thomas, G. E., and Stamnes, J. J.: Radiative Transfer in the Atmosphere and Ocean, chap. 3.3, p. 79, Cambridge University Press, 2017.

Warren, S. G.: Optical properties of ice and snow, Philosophical Transactions of the Royal Society A: Mathematical, Physical and Engineering Sciences, 377, 20180 161, 2019.

Yang, P., Bi, L., Baum, B. A., Liou, K.-N., Kattawar, G. W., Mishchenko, M. I., and Cole, B.: Spectrally Consistent Scattering, Absorption, and Polarization Properties of Atmospheric Ice Crystals at Wavelengths from 0.2 to 100 μm, Journal of the Atmospheric Sciences, 70, 330–347, 2013.